Radio Science, Volume 32, Number 6, Pages 2309–2320, November–December 1997

Imaging coherent backscatter radar observations of topside equatorial spread F

D. L. Hysell

Department of Physics and Astronomy, Clemson University, Clemson, South Carolina

R. F. Woodman

Instituto Geofísico del Perú, Lima

Abstract. Multiple baseline interferometric imaging of a large-scale topside spread F depletion has been performed at the Jicamarca Radio Observatory near Lima, Perú. A new imaging technique makes it possible to examine the detailed structure of the scatter from field-aligned irregularities in and around the depletion. A new antenna at Jicamarca, physically separated from the main antenna array, provided very long interferometry baselines up to $\sim 94\ \lambda$ long for the observations. High-resolution images of coherent backscatter from the radar plume were computed from the interferometry data using the maximum entropy method. These images show that scattering regions with small Doppler velocities lay mainly along the boundary of the depleted region. Meanwhile, regions with high Doppler velocities were located within the depletion itself and could be seen convecting upward through the depleted channel.

1. Introduction

This paper describes the application of a new radar imaging method to a case study of a large-scale plasma depletion observed during equatorial spread F conditions. The observations were made at the Jicamarca Radio Observatory, which has a modular phased array antenna ideally suited for multiple-baseline interferometry. Large-scale depletions have been studied for many years at Jicamarca using the coherent scatter radar technique, which relies upon the fact that small-scale density irregularities usually accompany the large-scale depletions. Within the spectrum of the irregularities are waves which match the Bragg scattering condition for the radar and give rise to strong backscatter. This scatter is termed "coherent" to distinguish it from much weaker "incoherent" or Thompson scatter. The coherent backscatter serves to some extent as a tracer of the morphology and dynamics of the unstable F region ionosphere and can be observed with quite fine range, temporal, angular, and Doppler resolution nowadays at Jicamarca. Examples of recent observations carried out at Jicamarca have been presented by *Farley and Hysell* [1996] and *Basu et al.* [1996].

Interpretation of the coherent scatter data is by no means straightforward. One complication is that the cause and nature of the small-scale irregularities themselves remains unknown. *Haerendel* [1973] and *Hudson et al.* [1973] originally hypothesized multistep processes with both interchange and drift wave instabilities taking part in the excitation of linearly damped small-scale waves. While this general view still has considerable support, detailed studies of various mechanisms that may be at work yielded mainly negative results (see for instance *Hudson and Kennel* [1975], *Chaturvedi and Kaw* [1976], and *Huba and Ossakow* [1979]). Hence we do not really know how the scattering irregularities relate to the large-scale waves in spread F; we do not know, for instance, to what extent their phase velocities, detected with the Doppler radar, represent real ionospheric plasma drifts. New theoretical developments appear to be waiting for more incisive observations.

Another factor complicating the interpretation of coherent scatter data is the very nature of radar ex-

Paper number 97RS01802.
0048-6604/97/97RS-01802$11.00

periments. Jicamarca uses a fixed antenna beam for transmission with a beam width of about 1°, limiting the spatial resolution transverse to the beam pointing position to roughly 10 km near the F peak. The radar cannot normally resolve spatial details with a transverse scale size comparable to or smaller than about 10 km. Considering that the finest height resolution of the Jicamarca radar is 125 m and that interesting vertical structure is apparent in the data at this resolution, it is easy to imagine that the poor transverse resolution of the radar skews the observations and suppresses important information about the structure and dynamics of the ionospheric flow.

Moreover, there is no way to distinguish temporal from spatial variations in the data. The nighttime F region ionosphere generally drifts eastward at speeds up to about v=200 m/s. The tendency has been to associate temporal changes occurring on a timescale τ with spatial variations in the scattering medium with scale size $\lambda_o = v\tau$, or to equate time with horizontal distance. (The same idea is employed in laboratory studies of turbulent flows, where length scales are measured by the time it takes for flow features to advect past stationary probes in a fluid.) However this assumes that the medium has not evolved substantially over the time τ, which is to say that the flow is frozen in. Now the preceding paragraph limited our observations to $\lambda_o \gtrsim 10$ km, implying $\tau \gtrsim 1$ min. This time, however, is at best not much smaller than the eddy turnover time of the individual large-scale depletions that characterize spread F [*Hysell*, 1992]. Making matters worse, v is typically both height and time dependent. The irregularities therefore are generally not frozen into the flow.

Radar interferometry offers a way to improve the spatial resolution of a radar experiment transverse to the line of sight and to distinguish the spatial and temporal evolution of the scattering medium. Using cross-correlation analysis of different receiving antennas, interferometry measures spatial structure within the scattering volume without appealing to the frozen-in flow hypothesis. Coherent scatter radar interferometry was introduced by *Farley et al.* [1981] and applied to spread F echoes by *Kudeki et al.* [1981]. The idea was that by statistically comparing the phase of the backscattered signals received on two spatially separated antennas, it is possible to measure the first three moments of the arrival angle distribution of the scatter with respect to the baseline that joins the antennas. In the case of field-aligned irregularities at the magnetic equator, this angle is just the zenith angle in the equatorial plane. Conventional interferometry with two antennas reveals (1) the total scattered power, (2) the mean arrival angle of the backscatter, and (3) the RMS width of the scattering angle distribution.

Then *Kudeki and Farley* [1989] pointed out that the classical interferometry technique can be generalized for more than two antennas and that additional antenna baselines convey higher-order moments of the scattering angle distribution. The moments specify an actual image of the scattering structure within the volume illuminated by the radar transmitter for each range and Doppler frequency. Multiple-baseline imaging interferometry is already widely applied in radio astronomy, sonar, and medical imaging but has not seen much use in atmospheric science (see *Thompson* [1986] for a review of most of the important concepts involved). *Kudeki and Sürücü* [1991] and *Sürücü and Kudeki* [1992] first applied the technique to studies of the equatorial electrojet and bottomside equatorial spread F. Recently, *Hysell* [1996] improved the resolution of the technique still further by employing a maximum entropy algorithm to the image inversion process [*Jaynes*, 1982]. The technique was used to investigate bottomside spread F, a phenomenon associated with intermediate-scale collisional interchange mode waves [*Zargham and Seyler*, 1987].

This paper presents the first coherent scatter observations of a large-scale spread F plasma depletion (plume) using the multiple-baseline imaging technique. The data were taken at Jicamarca, which has just undergone an upgrade, extending its longest interferometry baseline to approximately 94 wavelengths. (The resolving power of imaging interferometry depends on the length of the longest baselines, which is relatively easy to increase, rather than on the size of the main antenna array, which is not!) High-resolution images of the backscatter distribution were computed from the interferometry data with the help of the MaxEnt algorithm. Doppler information has been encoded in the images. The imaging technique offers a more incisive, less ambiguous means of studying plasma waves with coherent scatter radar. The added information it brings could motivate new theories of the origin of small-scale scattering irregularities in the disturbed F region ionosphere.

2. Experimental Setup

Figure 1 shows a schematic view of the Jicamarca antenna array. The main array is oriented 6°1' east of north so as to be aligned with the geomagnetic field circa 1960. (Presently, the geomagnetic field declination in Perú is only about 20' east of north.) It consists of eight independent antennas: four quarters with two linear polarizations each. Transmission and reception can be done using combinations of these eight antennas, connected and phased through hybrid networks. Beam pointing positions are selected by phasing the modules (64ths) of the array with precut cables. These modules can also be disconnected and used independently for reception. During our experiments, linearly polarized signals were transmitted from the north and south quarters of the array which were phased so as to point perpendicular to B. The transmission half-power full beam width in the equatorial plane was approximately 2°.

A duplicate of one of the Jicamarca modules was recently constructed to the west of the main array. A distance of 203.73 m, precisely 4 times the diagonal width of a module, lies between the centers of the new module and the westmost of the old modules along a line bisecting the main array. (The new antenna is located precisely 71.75 m magnetic south of that line.) The purpose of the new antenna is long-baseline interferometry. For our experiments, the five modules shown were used for reception. They were not collinear and need not be; since the *F* region irregularities are field-aligned, the contours of constant correlation measured on the ground will be highly elongated in the magnetic north-south direction. The problem is inherently one-dimensional, and only the perpendicular projection of the displacements between antennas is important. By using the five modules shown, interferometry can be performed with 10 nonredundant baselines, with nonredundant spacings lying between 1 and 11 module widths (~51–560 m) projected on a line transverse to **B**. These particular modules were chosen to give an approximately uniform distribution of baseline lengths.

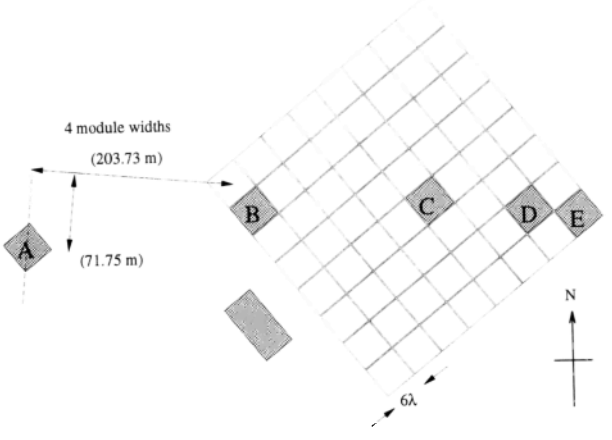

Figure 1. Layout of the Jicamarca antenna array. The main antenna is a phased array of dipoles that can be subdivided into 64 modules. A new module was constructed to the west of the main antenna.

At present, only four receivers can be digitally sampled at Jicamarca. (An upgrade to remedy this situation is under way.) Analog switching was therefore used for our experiments to multiplex one receiver between antennas B and C from Figure 1. The switch alternated between the two antennas every 16 transmitter pulses. This means that the signals from these two antennas could not be cross correlated and that all the cross-correlation measurements involving either antenna will receive only half the number of incoherent integrations of the others. It also means that power spectra with better than 16-point resolution cannot be computed from the data. In this paper, we will present only 4-point spectral computations (see the Data Presentation section).

3. Data Analysis Techniques

Figure 2 is a conventional range time intensity (RTI) plot of a topside plume observed on April 13, 1996. It shows the signal-to-noise ratio of the backscattered signal received by the new antenna module. The radar plume emerged suddenly, about 5 min before the data recording commenced, and was not preceded by bottomside spread *F*. We missed recording the onset of the event as well as the high-altitude portion before about 2025 LT. Problems with the data acquisition system also occurred between 2017 and 2025 LT. The RTI plot nevertheless still conveys a typical topside plume rising over a bottomside spread *F* layer. However, interpretation of the RTI image is perilous because of the factors outlined above.

The signal and noise powers and power spectra for all five antennas were computed, along with the normalized cross spectra for all antenna pairings excluding B-C (nine pairings in all). These measurements constitute a discrete estimate of the spatial

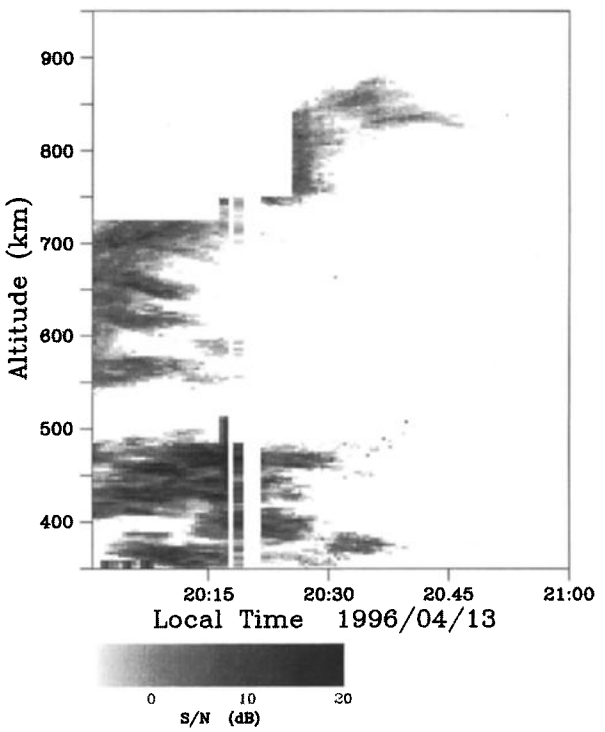

Figure 2. Range-time-intensity plot of the radar plume. Signal-to-noise ratios in decibels are coded as gray scales.

cross spectrum of the scattered signal on the ground, which can be shown to be the Fourier transform of the backscatter arrival angle distribution [*Thompson*, 1986].

$$g(kd,\omega) = \int \frac{d\psi}{\sqrt{1-\psi^2}} f(\psi,\omega)A(\psi)e^{ikd\psi} \quad (1)$$

$$g(kd,\omega) \rightleftharpoons f(\psi,\omega)A(\psi) \quad (2)$$

Here g is the complex spatial cross spectrum or visibility function of the scattered signal on the ground, k is the radar wavenumber, d is the antenna separation distance perpendicular to the magnetic meridian, ω is the Doppler frequency, f is the arrival angle or brightness distribution of the backscatter, and ψ is the direction cosine defined by the wave vector and baseline and may be thought of as the zenith angle in the equatorial plane. (The terms "brightness" and "visibility" are commonly used by the radio astronomy community [*Thompson*, 1986].) The narrow transmitter beam width assures that we need only consider small values of ψ in the integral and also permits us to sample g discretely. Note that the scattered signal is stochastic in nature and that both f and g are time-averaged quantities. The function A is the transmitting antenna radiation pattern. We have neglected the receiving antenna pattern, which is much broader by comparison.

The goal of interferometric imaging is to compute $f(\psi,\omega)$ in each radar range gate for each incoherent integration period. From the brightness distributions, we can construct high-resolution images of the radar backscatter in which time and space are independent axes.

Our data supply estimates of g at nine nonredundant baseline lengths whose ratios are 1:2:3:4½:5½:6½:8:10:11. Obviously, g has been nonuniformly sampled in this instance. (Means of Fourier analyzing such data are described by *Marvasti* [1993] among others.) More important, it has been incompletely sampled; the coherence even with the longest baseline can often be near unity, implying that even longer baselines would contain useful information about the structure of the backscatter.

To compute a discrete estimate of the brightness distribution $f(\psi,\omega)$ from our incompletely sampled data, we have turned to a maximum entropy approach used widely in radio astronomy [*Ables*, 1974]. Maximum entropy methods have their foundations in information theory and Bayesian statistics and represent a popular approach to generalized inversion theory [*Jaynes*, 1985]. We can also think of the maximum entropy method as a model-based inversion process, where the model for $f(\psi,\omega)$ is a positive definite, maximally smooth (in one sense) function constrained to be consistent with the data $g(kd,\omega)$, to a specified accuracy [*Press et al.*, 1988]. Numerous reviews and rationales have been given for the maximum entropy method, few more eloquent than *Jaynes* [1982], *Jaynes* [1985], and *Skilling* [1991].

We use the MaxEnt algorithm described by *Jaynes* [1982] to estimate the brightness spectrum by maximizing its Shannon entropy [*Shannon and Weaver*, 1949] at each Doppler frequency ($S_\omega = -\int d\psi f(\psi,\omega) \ln f(\psi,\omega)/F$) subject to the constraints imposed by the visibility data. The constraints must take statistical and self errors into account. Here F refers to the total signal power, and ψ refers to the arrival angles included in the image. The problem can be formulated as a system of n coupled nonlinear equations, where n is twice the number of interferometry baselines plus one (there being two complex visibility data per baseline plus one for the zero lag, n=19 in this case). Implementing the MaxEnt algorithm

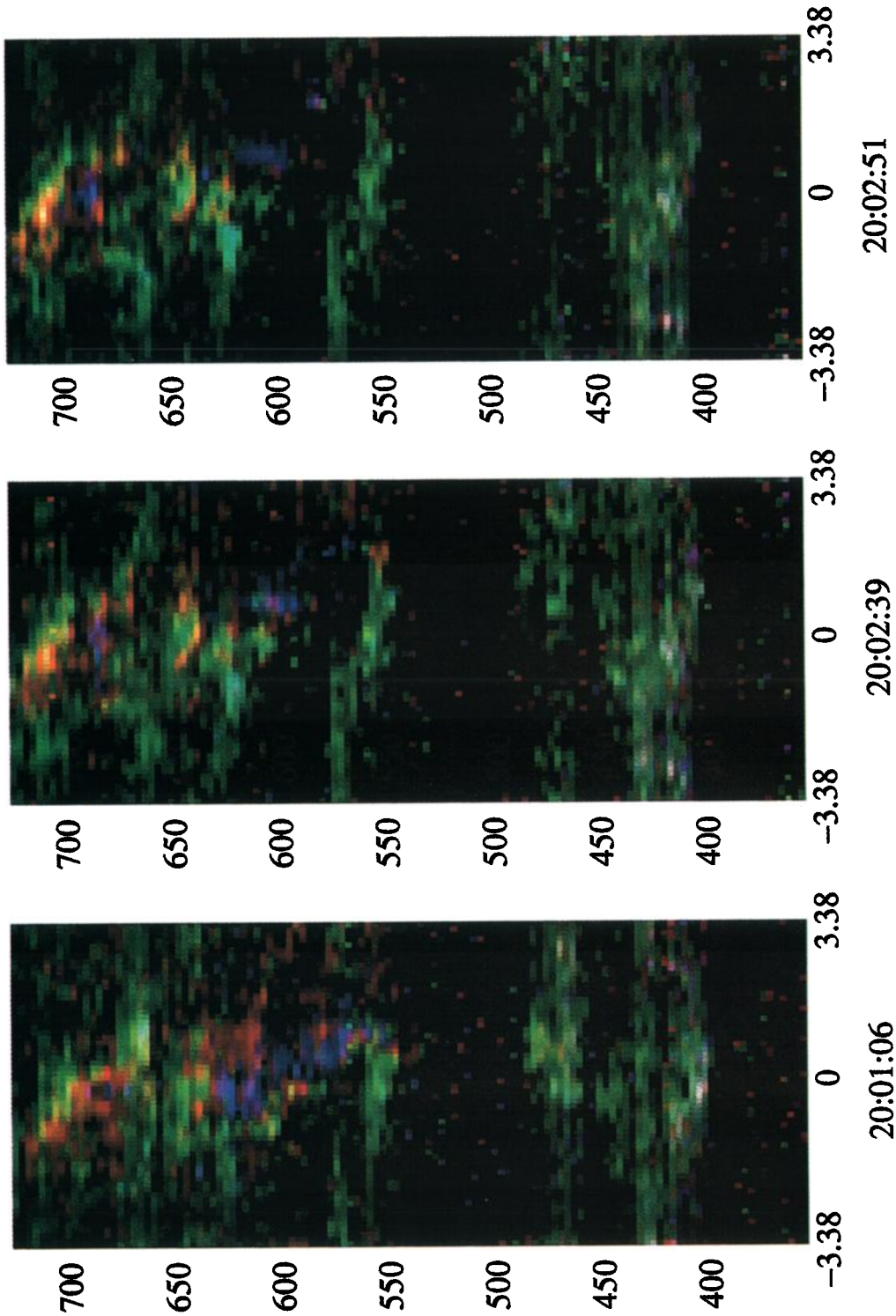

Plate 1. Images computed from all available baselines at two different times. Doppler information is encoded in the pixel colors. The green components have small Doppler velocities, and the red and blue components have Doppler velocities nominally corresponding to ascent and decent, respectively. In fact, the data are frequency aliased, and most of the blue patches are ascending very rapidly. Color intensities signify signal-to-noise ratios from 0 to 25 dB.

amounts to solving these equations numerically for each range gate at each Doppler frequency.

Details of the basic algorithm and mathematical derivations presented here were given by *Hysell* [1996, and references therein]. We start by relating a measurement of a component of the visibility g_j at some antenna spacing d_j, together with the error of the measurement e_j, to the brightness distribution

$$g_j + e_j = \int d\psi f(\psi)\cos(kd_j\psi) \quad (3)$$

$$g_j + e_j = \int d\psi f(\psi)\sin(kd_j\psi) \quad (4)$$

$$g_j + e_j = \int d\psi f(\psi)h_j(\psi) \quad (5)$$

where $h_j(\psi)$ is the interferometer point spread function and is either sine or cosine depending on whether g_j is a real or imaginary component. Note that the continuous functions of ψ shown above can be discretized in practice. Casting the maximum entropy problem as one in variational mechanics, where each of the constraints associated with $j = 1, ..., n$ data points enters with a Lagrange multiplier λ_j, motivates us to express the brightness distribution in the following way:

$$f(\psi) = Z^{-1}Fe^{-\lambda_j h_j(\psi)} \quad (6)$$

$$Z = \int d\psi e^{-\lambda_j h_j(\psi)} \quad (7)$$

where the Einstein summation convention is in play (like indices are summed). In terms of (6), the entropy of the brightness distribution may now be written as

$$S(f) = \lambda_j(g_j + e_j) + F\ln Z + \Lambda\left(e_j C^{-1}_{jk} e_k - \Sigma\right) \quad (8)$$

which will be maximized through a process of differentiation with respect to the n Lagrange multipliers and n error terms. In order to bound the size of the error terms and in the spirit of variational mechanics, we introduce a constraint on the residual of the errors (Σ) along with yet another Lagrange multiplier Λ. C^{-1} is the inverse covariance matrix of the errors. The philosophy here is to let the algorithm travel uphill in the direction of maximum entropy as far as the expected norm of the errors permits, preventing it from producing lower-entropy images fraught with statistical artifacts. The Σ parameter is nominally set to equal the expectation of the term it shares brackets with but may be varied, the effect on the images being like that of turning a contrast control.

Differentiating (8) with respect to λ_j relates the visibility estimates and errors to the brightness distribution. This gives us n coupled nonlinear equations in the n Lagrange multipliers that must be solved numerically. Differentiating with respect to e_j gives a matrix equation which is a recipe for deriving the error terms from the Lagrange multipliers. Finally, differentiating with respect to the final Lagrange multiplier Λ allows us to solve for it in terms of the others. We solve the equations with a globally convergent Newton method which requires us to compute and invert an $n \times n$ Jacobian matrix. It should be noted that computing this matrix by finite differences is no more computationally expensive than doing so analytically and leads to a more robust algorithm overall.

Hysell [1996] neglected the fact that errors in the visibility estimates for different baselines are correlated in general if the baselines share a common antenna. The case of correlated errors has been discussed in some detail by E. Kudeki et al. in a manuscript in preparation and has also been addressed in the context of incoherent scatter autocorrelation function measurements by *Huuskonen and Lehtinen* [1996]. We adopt their approach here, basing the error constraint in (8) on the full covariance matrix. In practice, it may be computationally expedient to first diagonalize C^{-1} by a similarity transformation, defining $e_j = A_{jk}e'_k$, where A is a matrix whose columns are the eigenvectors of C^{-1} and e'_k are the errors in a space where the covariance matrix is diagonal.

The elements of the covariance matrix have been estimated by *Farley* [1969] for the case of real samples and in the context of multipulse autocorrelation function measurements. His variance estimates were recently generalized for complex samples by *Farley and Hysell* [1996]. For the sake of completeness, we have generalized the covariance terms for the case of complex samples and for both high and low signal-to-noise ratios and coherence levels. The more general expressions are given by

$$\langle(\rho_1 - \langle\rho_1\rangle)(\rho_2 - \langle\rho_2\rangle)^*\rangle =$$
$$\frac{1}{k}\left(\frac{S+N}{S}\right)^2\left[\rho_3^*\frac{S}{S+N} - \rho_1\rho_2^*\left(\frac{S}{S+N} - \frac{1}{4}\right)\right.$$
$$- \frac{1}{2}\left(\frac{S}{S+N}\right)^2\left(|\rho_1|^2 + |\rho_2|^2\right)\rho_3^*$$
$$\left. + \frac{1}{4}\left(\frac{S}{S+N}\right)^2\left(|\rho_1|^2 + |\rho_2|^2 + |\rho_3|^2\right)\rho_1\rho_2^*\right] \quad (9)$$

in which $\rho_1 = \rho(d_1)$, $\rho_2 = \rho(d_2)$, and $\rho_3 = \rho(d2 - d1)$ are normalized complex spatial cross-correlation measurements and S and N refer to the signal and noise power levels, respectively. Here k refers to the number of statistically independent samples. We assumed here that the sky noise received on different antennas is totally uncorrelated. We have also assumed that many more noise samples exist than signal samples and that the errors in the noise estimators used for normalization are therefore negligible. Note that (9) applies to pairs of cross-correlation measurements made with a common antenna at an endpoint. In the case of pairs of measurement sharing an antenna at their midpoint, the expression takes a slightly different form.

$$\langle(\rho_1 - \langle\rho_1\rangle)(\rho_2 - \langle\rho_2\rangle)^*\rangle =$$
$$\frac{1}{k}\left(\frac{S+N}{S}\right)^2\left[\rho_1\rho_2^*\left(\frac{S}{S+N} - \frac{1}{2}\right)^2\right.$$
$$- \frac{1}{2}\left(\frac{S}{S+N}\right)^2\left(\rho_1^2\rho_3^* + \rho_2^{*2}\rho_3\right)$$
$$\left. + \frac{1}{4}\left(\frac{S}{S+N}\right)^2\left(|\rho_1|^2 + |\rho_2|^2 + |\rho_3|^2\right)\rho_1\rho_2^*\right] \quad (10)$$

in which $\rho_3 = \rho(d1 + d2)$ this time. Errors for different cross-correlation measurements made with distinct sets of antennas are uncorrelated. From these expressions, we can compute the complete covariance matrix for the imaging experiments and, from it, the linear transformation that relates the usual error terms to the errors in the basis where the inverse covariance matrix is diagonal. It is a straightforward matter to extend the result to the case where the real and imaginary components of the errors are dealt with separately.

The covariance matrix is generally diagonally dominant in cases of low signal-to-noise ratios or low visibilities. Statistical errors tend to be poorly correlated when the correlation functions themselves are computed from noisy data or are otherwise small. In such cases, the covariance matrix may be well approximated by its diagonal terms alone. As signal-to-noise ratios increase, the diagonal terms given by *Farley and Hysell* [1996] diminish faster than the off-diagonal terms, becoming comparable when visibilities are high and the signal-to-noise ratio is greater than a few times unity. Even in this case, however, the inclusion of off-diagonal terms in the computation often brings about only subtle changes in the final image.

4. Data Presentation

Figure 3 shows four examples of images computed from the interferometry data. The vertical axis represents range (altitude), and the horizontal axis represents zenith angle, from ±3.38°. The vertical resolution of the images is 3 km, and the horizontal resolution is 0.1°, about 1 km at 550-km altitude and about one twentieth the transmitter antenna beam width. Every row in an image represents the brightness distribution calculated from the data from one range gate. The background noise level was estimated for each image from the power profiles received on all the antennas and subtracted from the zero lags of the visibility data before the brightness was computed. The brightness distributions were then divided by the noise level. Gray scales show the signal-to-noise ratio in decibels, with values spanning 0–25 dB. Each image has been incoherently integrated for 6 s. From left to right, these panels show images of the scattering volume computed with data from two (D and E), three (C, D, and E), four (B, C, D, and E), and all five (A through E) antennas. The number of baselines going into the image are then one, three, five, and nine, with the length of the longest baseline approximately doubling each time. The figure is meant to illustrate how interferometry can resolve structures within the scattering volume and how the detail increases with increasing visibility data. Three baselines give a much clearer image of the radar target than two. With nine baselines, we have a precise map of just where within the radar beam scattering is taking place.

In the topside region above 500 km, much of the backscatter seems to fall along two diagonal lines (which have been highlighted). The scatter from the line on the right (toward the east or top) is stronger than that from the left. Additional strong, diffuse scatter seems to be coming from the volume between

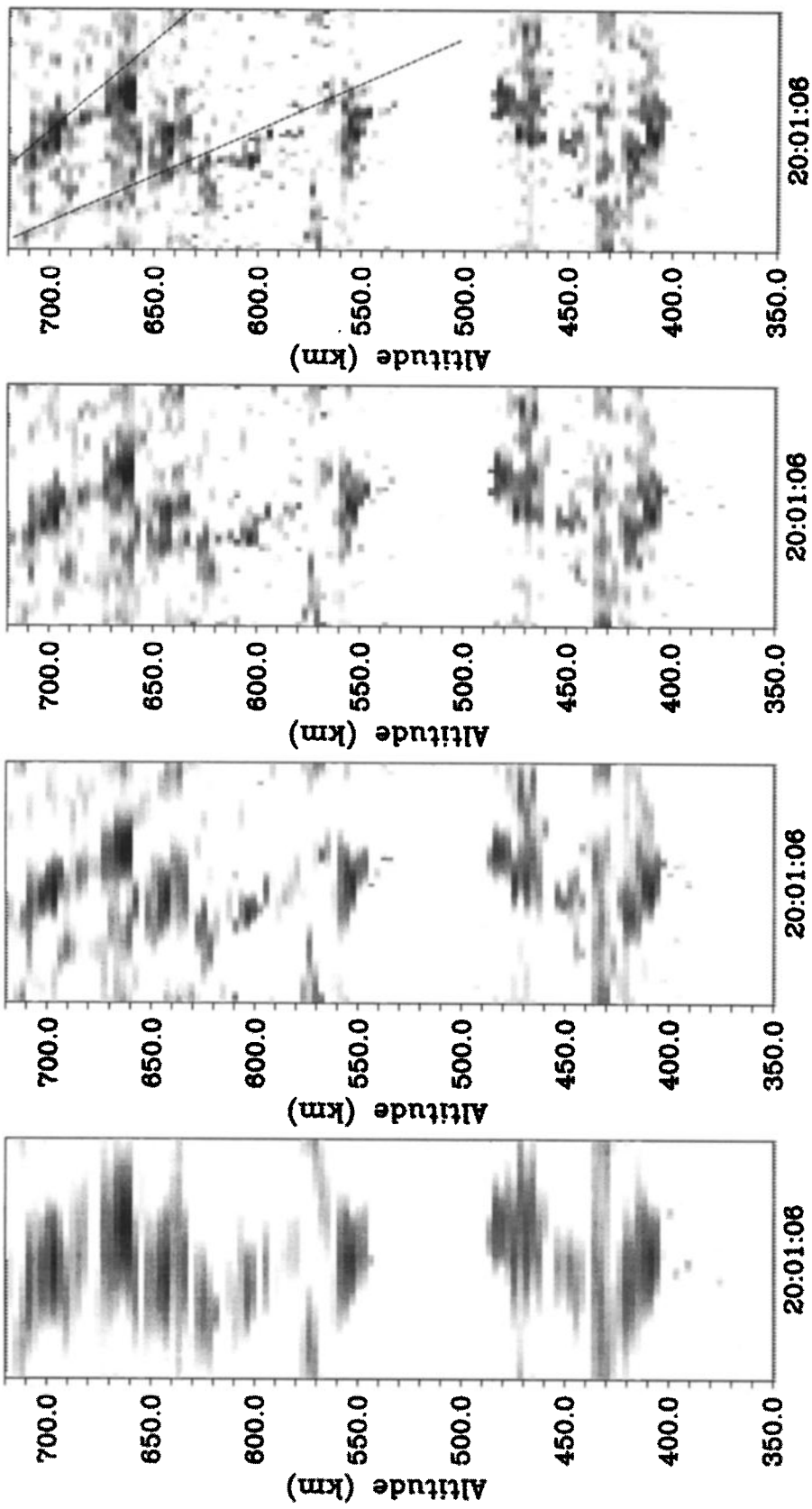

Figure 3. Four panels showing the results of interferometric imaging for a progressively increasing number of baselines (from left to right, one, three, five, and nine). The horizontal axes represent zenith angles in the equatorial plane from ±3.38°. East is to the right. The vertical axes represent altitude, and the gray scales depict signal-to-noise ratios from 0 to 25 dB. The data were integrated for 6 s. The images shown were derived entirely from the zero Doppler frequency components of the visibility data.

the lines and from a small "tail" at 550 km altitude. Additional backscatter comes from a bottomside spread F layer between 400 and 500 km.

Note that no range correction to the power was applied when generating the images. Nor has the antenna pattern $A(\psi)$ been removed from them. The tendency for the scatter coming from zenith to be more intense than that coming from the periphery is a reflection of transmitter beam weighting. Some angle aliasing is still taking place in the picture, even though the minimum baseline length is much smaller than the antenna width, due to the tremendous dynamic range of the target. Furthermore, it is likely that irregularities at low altitudes produce phase scintillations in backscatter from higher altitudes, causing deviations in the observed arrival angles. Unlike the images of *Hysell* [1996], these images do not show very clear sidelobe patterns or nulls. This is due in part to the use of a special cabling arrangement at Jicamarca which effectively tapered the excitation across the transmitting antenna, filling in the normal nulls and spreading the tails of the radiation pattern across the angles shown in our images. Angle aliasing and scintillations contribute further to poorly defined nulls. We reiterate that image components falling well outside the 2° half-power full beam width of the transmitting antenna remain visible even in the periphery due to the huge dynamic range of the target.

An ordinary coherent scatter radar experiment makes observations in a space with three coordinate axes: range, time, and Doppler frequency. Multiple-baseline radar interferometry incorporates information about the diffraction pattern of the signal on the ground to add a fourth independent axis, representing arrival angle, to that space. The technique makes optimal use of all available data in some sense to produce images which do not suffer from spatial-temporal ambiguities. However it also presents a problem for visualization. Just how do you view a four-dimensional data set?

The time axis may be dealt with by viewing sequential radar images in animated form. While this method does not lend itself to journal format, it is ideally suited for the World Wide Web. (Readers may consult our home page at http://landau.phys.clemson.edu to view animated versions of the data discussed here.) In this paper, we merely present data from different times in separate images. Of the remaining dimensions, at least some of the Doppler information may be represented in conventional two-dimensional images alongside the scattering intensity with some use of color. In every range/zenith-angle pixel in the image, for example, the zeroth, first, and second moment of the Doppler spectrum could be used to set the brightness, hue, and saturation of the pixel.

Another possibility, which we have followed here, is to assign different image colors to different brightness Doppler bins. We have spectrally analyzed the radar data using a four-point discrete Fourier transform. Visibility spectra were computed separately for each of the four Doppler components. The reason for the four-point transform is simply that our final images ultimately have only three degrees of freedom in each pixel (red, green, and blue) and that we know of no way to integrate more detailed Doppler data into our images. Four images like the rightmost in Figure 3 were computed from the visibilities. The image corresponding to the positive Doppler frequency bin was coded blue (for blue shifted echoes), the zero frequency bin was coded green, and the negative frequency bin was coded red (for red shifted echoes). The fourth remaining, high-frequency spectral component was color-coded magenta, a color combination that occurs seldom in practice otherwise. All four images were then digitally summed to produce the color maps shown in Plate 1. The pulse-repetition frequency for our experiments was 150 Hz, meaning that we can resolve Doppler velocities between ±225 m/s without aliasing.

Plate 1 shows three radar images separated in time by almost 2 min and then by a few seconds. The image on the left is a replica of the one in Figure 3, only this time including Doppler information. The color of each pixel is just the linear combination of the red, green, and blue components. Blue patches normally suggest descent, and red suggests ascent. Green patches suggest no line-of-sight motion, while white patches suggest broad Doppler spectra and hence strong turbulence. Frequency aliasing is a strong possibility, and most of the blue and magenta patches should be associated with large negative Doppler shifts in this case (with rapid ascent).

We can now see that the diagonal lines from Figure 3 are mostly green, while the more diffuse scatter between them is mostly red. We interpret the green lines as signifying the boundaries of a large-scale depletion wedge, a boundary which is not expected to deform at very high speed. (Since electric fields, wave vectors, and density gradients are all parallel for electrostatic waves, streamlines of the flow should be

nearly tangent to the depleted channel boundaries, making those boundaries essentially fixed.) Steep plasma density gradients occur along this boundary and are evidently the site of small-scale plasma density irregularities. The fact that the upper boundary (where $\partial n/\partial z > 0$) gives rise to stronger backscatter may be a reflection of its gravitational instability. We expect that the boundaries extend all the way down to the bottomside F region, even if the coherent scatter from them does not.

Meanwhile, the scattering regions exhibiting significant Doppler velocities lie between the boundaries as if convecting upward between them. The regions with the largest Doppler shifts of all lie near the base of the depletion channel around 550–600 km. They are colored blue and cyan but are in fact frequency aliased and possess large negative Doppler shifts (see below). The image seems to be consistent with the "chimney" picture of large-scale plasma depletions [*Woodman and La Hoz*, 1976; *Hysell et al.*, 1994]. The idea is that a developed depletion wedge presents a kind of one-dimensional geometry where only horizontal Pedersen and polarization currents come into play. Polarization charges that develop at the walls of the depletion cannot easily be discharged by currents outside the depletion, which would have to close over the distant top of the radar plume or through the poorly conducting valley region below. They must therefore be discharged directly by currents inside. Since the conductivity is poor where the plasma density is low, however, the electric field in the depleted channel must become quite large to sustain the current. Regions of depleted plasma then rapidly $\mathbf{E} \times \mathbf{B}$ drift upward into the wedge with a speed greater than the rate at which the depletion boundary itself can move. We expect the plasma convection speed to be greatest near the base of the depletion since polarization charges there are almost completely inhibited from being discharged by Pedersen currents flowing above or below.

We have animated a series of 275 images like Plate 1 and verified that the high-Doppler scattering regions generally do ascend through the topside channel with speeds roughly consistent with their Doppler shifts, assuming that regions with seemingly positive Doppler shifts are in fact frequency aliased. Apparent vertical advection speeds as high as about 400 m/s are evident in a few localized regions, in agreement with the dealiased Doppler speeds. The channel itself moves eastward at approximately 170 m/s, as deduced from its left-to-right motion in time in our animations. The topside region shows considerable vertical shear, giving rise to a familiar westward tilt of the radar plume. The bottomside F region seems to be moving eastward somewhat more rapidly than the topside, but the layer itself is shear-free. We note that the absence of shear prevents us from discerning much structure in the bottomside region below 500 km, intermediate-scale interchange mode waves being too small to resolve without shear to increase the dominant wavelength of the instability.

By comparison with the leftmost panel, the central and rightmost panels in Plate 1, taken later, exhibit a few important features that hint at the time evolution of the large-scale depletion. These include (1) a more acute westward tilt due to sheared flow and (2) the upward displacement of some of the high Doppler regions inside the depleted channel. The fast rising scattering regions have relatively short lifetimes of perhaps tens of seconds. To observe their upward displacement in time, one must compare the rightmost two panels in Plate 1, which are separated in time by only 12 s, or about enough time for the fastest moving regions to ascend by one range gate. Interestingly, the scattering regions with small Doppler velocities have much longer lifetimes and persist long enough to be followed for several minutes as they pass through the radar beam.

The central and rightmost panels in Plate 1 also exhibit (3) an emerging view of large-scale vertical structuring of the westward wall of the depletion. This structuring seems to be evidence of a secondary, zonal wind-driven interchange instability with a vertical wavelength of about 50 km. Such secondary features have been described and reported on by *Tsunoda et al.* [1982] but have not been observed before with the kind of spatial and temporal resolution permitted by our imaging technique. The bifurcations or tails produced by the secondary instability lag behind the main vertical channel, presumably under the influence of vertical polarization electric fields generated by the secondary instability. They are responsible for the horizontal streaks in Figure 2 between 550 and 700 km that give it its "plume-like" or even "rooster tail" appearance. Rooster tails are characteristic of many of the topside spread F events recorded at Jicamarca, but it has never been clear whether the streaks signified physically elongated features or just isolated scattering blobs suspended over the radar for long periods of time. In this case, we find that they have both qualities.

5. Summary and Conclusions

Radar imaging with multiple-baseline interferometry offers a new, more incisive way of observing coherent scatter from plasma irregularities. There is a price to be paid in the form of reduced sensitivity (only a small fraction of the Jicamarca main antenna is used for reception) and the increased computational cost of data analysis. In return, the technique produces high-resolution images in which space and time are independent parameters. The data presented here seem to confirm some long-held but loosely supported theories about large-scale plasma depletions: that their boundaries are highly structured and can be the source of VHF coherent scatter, that the highest Doppler speeds are observed in regions within depleted channels, that high Doppler velocities at least sometimes correspond to bulk plasma motion, and that radar plumes signify secondary instabilities.

The main impediment to the interpretation of the coherent scatter data from Jicamarca over the past few years has been the complexity of the problem and, in particular, the inability to sort temporal and spatial effects. Doppler spectra from topside spread F are notoriously complex, for instance, presumably because of the effects of spatial superposition [*Woodman and La Hoz*, 1976]. We now have a means of computing Doppler spectra for particular scattering regions in space. It should be possible now to relate the spectral shapes with the motion of the regions they represent.

There are a number of steps we could take to further improve the quality of the images from Jicamarca. Adding the capacity to sample more than four receivers will essentially double the data rate of the imaging experiments described here, improving the statistics of the visibility measurements and clarifying the images substantially. At present, we use a self-calibration technique to calibrate the relative phases of the receiving system at Jicamarca. This technique involves searching through the space of phase offsets to find the combination yielding the image with the highest overall entropy. An independent calibration using radio stars or satellites would be more accurate and lead to clearer images (since errors in the phase offsets result in blurring). The use of an additional, shorter interferometry baseline would help reduce angle aliasing in the images and so help suppress artifacts. This is an especially important concern when imaging bottomside spread F layers which tend to have a broad zonal extent. A shorter baseline can easily be included in the measurements by sampling two antenna modules directly adjacent to one another. At this point, the zonal resolution of the imaging technique is limited by the motion of the radar target across the interferometer during each incoherent integration. The integration time here (6 s) was chosen so that the F region irregularities traverse at most one pixel during the integration. We can sharpen the images while leaving the integration time constant by introducing progressive phase shifts into the raw radar data so as to freeze the target in zenith angle. Finally, real estate is hardly scarce at Jicamarca, and additional antennas could be constructed to further lengthen the interferometry baselines if important features in the scattering medium remain unresolved.

Acknowledgments. The authors gratefully acknowledge helpful input from E. Kudeki and J. D. Sahr. This work was supported by the National Science Foundation through cooperative agreements ATM-9022717 and ATM-9408441 and by NSF grants ATM-9415931 and ATM-9424550. The Jicamarca Radio Observatory is operated by the Geophysical Institute of Perú, Ministry of Education, with support from the NSF cooperative agreements just mentioned. The help of the staff, particularly those who took part in construction of the new antenna, was much appreciated.

References

Ables, J. G., Maximum entropy spectral analaysis, *Astron. Astrophys. Suppl. Ser.*, *15*, 383, 1974.

Basu, S., et al., Scintillations, plasma drifts, and neutral winds in the equatorial ionosphere after sunset, *J. Geophys. Res.*, *101*, 26,795, 1996.

Chaturvedi, P. K., and P. Kaw, An interpretation for the power spectrum of spread F irregularities, *J. Geophys. Res.*, *81*, 3257, 1976.

Farley, D. T., Incoherent scatter correlation function measurements, *Radio Sci.*, *4*, 935, 1969.

Farley, D. T., and D. L. Hysell, Radar measurements of very small aspect angles in the equatorial ionosphere, *J. Geophys. Res.*, *101*, 5177, 1996.

Farley, D. T., H. M. Ierkic, and B. G. Fejer, Radar interferometry: A new technique for studying plasma turbulence in the ionosphere, *J. Geophys. Res.*, *86*, 1467, 1981.

Haerendel, G., Theory of equatorial spread F, re-

port, Max-Planck-Inst. für Phys. und Astrophys., Garching, Germany, 1973.

Huba, J. D., and S. L. Ossakow, On the generation of 3-m irregularities during equatorial spread *F* by low-frequency drift waves, *J. Geophys. Res.*, *84*, 6697, 1979.

Hudson, M. K., and C. F. Kennel, Linear theory of equatorial spread *F*, *J. Geophys. Res.*, *80*, 4581, 1975.

Hudson, M. K., C. F. Kennel, and P. K. Kaw, A two-step drift mode theory of equatorial spread *F* (abstract), *Eos Trans. AGU*, *54*, 1147, 1973.

Huuskonen, A., and M. S. Lehtinen, The accuracy of incoherent scatter measurements: Error estimates valid for high signal levels, *J. Atmos. Terr. Phys.*, *58*, 453, 1996.

Hysell, D. L., On the hierarchy of processes contributing to equatorial spread *F*, Ph.D. thesis, Cornell Univ., Ithaca, N. Y., 1992.

Hysell, D. L., Radar imaging of equatorial *F* region irregularities with maximum entropy interferometry, *Radio Sci.*, *31*, 1567, 1996.

Hysell, D. L., M. C. Kelley, W. E. Swartz, and D. T. Farley, VHF radar and rocket observations of equatorial spread *F* on Kwajalein, *J. Geophys. Res.*, *99*, 15,065, 1994.

Jaynes, E. T., On the rationale of maximum-entropy methods, *Proc. IEEE*, *70*, 939, 1982.

Jaynes, E. T., Where do we go from here?, in *Maximum-Entropy and Bayesian Methods in Inverse Problems*, edited by C. R. Smith and W. T. Grandy Jr., chap. 2, pp. 21-58, D. Reidel, Norwell, Mass., 1985.

Kudeki, E., and D. T. Farley, Aspect sensitivity of equatorial electrojet irregularities and theoretical implications, *J. Geophys. Res.*, *94*, 426, 1989.

Kudeki, E., and F. Sürücü, Radar interferometric imaging of field-aligned plasma irregularities in the equatorial electrojet, *Geophys. Res. Lett.*, *18*, 41, 1991.

Kudeki, E., B. G. Fejer, D. T. Farley, and H. M. Ierkic, Interferometer studies of equatorial *F* region irregularities and drifts, *Geophys. Res. Lett.*, *8*, 377, 1981.

Marvasti, F., Nonuniform sampling, in *Advanced Topics in Shannon Sampling and Interpolation Theory*, edited by R. J. Marks, chap. 4, pp. 121–156, Springer-Verlag, New York, 1993.

Press, W. H., B. P. Flannery, S. A. Teukolsky, and W. T. Vetterling, *Numerical Recipes in C*, Cambridge Univ. Press, New York, 1988.

Shannon, C. E., and W. Weaver, *The Mathematical Theory of Communication*, Univ. of Ill. Press, Urbana, 1949.

Skilling, J., Fundamentals of MaxEnt in data analysis, in *Maximum Entropy in Action*, edited by B. Bucks and V. A. Macaulay, chap. 2, pp. 19–40, Clarendon, Oxford, England, 1991.

Sürücü, F., and E. Kudeki, Radar imaging studies of bottomside equatorial spread *F*, paper presented at the Coupling, Energetics, and Dynamics of Atmospheric Regions workshop, Boulder, Colo., June, 1992.

Thompson, A. R., *Interferometry and Synthesis in Radio Astronomy*, John Wiley, New York, 1986.

Tsunoda, R. T., R. C. Livingston, J. P. McClure, and W. B. Hanson, Equatorial plasma bubbles: Vertically elongated wedges from the bottomside *F* layer, *J. Geophys. Res.*, *87*, 9171, 1982.

Woodman, R. F., and C. La Hoz, Radar observations of *F* region equatorial irregularities, *J. Geophys. Res.*, *81*, 5447, 1976.

Zargham, S., and C. E. Seyler, Collisional interchange instability, 1, Numerical simulations of intermediate-scale irregularities, *J. Geophys. Res.*, *92*, 10,073, 1987.

D. L. Hysell, Department of Physics and Astronomy, Clemson University, Clemson, SC 29634-1911. (e-mail: daveh@vlasov.phys.clemson.edu)

R. F. Woodman, Radio Observatory de Jicamarca, Apartado 13-0207, Lima 13, Perú. (e-mail: ron@geo.igp.gob.pe)

(Received January 10, 1997; revised May 22, 1997; accepted June 20, 1997.)